Geophysical Research Letters

Supporting Information for

Sensitivity of Modeled Elastic Deformation in the Amundsen Sea Embayment

J. S. Hansen[1,2], W. J. Durkin[3], M. J. Willis[1,2,4], T. J. Wilson[3], M. G. Bevis[3], D. D. Gómez[3]

[1] Department of Geological Sciences, University of Colorado Boulder

[2] Cooperative Institute for Research in Environmental Sciences

[3] School of Earth Sciences, The Ohio State University

[4] Department of Geosciences, Virginia Tech

Contents of this file

Additional Supporting Information (Files uploaded separately)

Introduction

We provide further information regarding the production of high-resolution grids of surface change in West Antarctica, including information about coregistration and grid uncertainties. We also provide full elastic modeling results and uncertainties. Finally, we provide a detailed description of ANET-POLENET GNSS processing and maps of surface changes occurring within 5 km of ANET-POLENET GNSS sites.

Text S1. Dynamic Coregistration and Surface Change grid Uncertainties

As a result of the lack of bedrock outcrops across much of the ASE region suitable for static registration points, we identify additional locations suitable for coregistration of DEM strips from the Reference Elevation Model of Antarctica (REMA) (Howat et al.,

2019). We extract these coregistration points from an 8m DEM mosaic available as part of REMA that we filter by long term vertical and horizontal velocities (from the NASA MEaSUREs velocity product (Mouginot et al., 2012; Rignot et al., 2011) and ICESat-ICESat-2 long term record of surface change (Smith et al., 2020). The higher the allowable threshold applied to the vertical and horizontal datasets, the more reference points become available for coregistration. However, enabling coregistration over 'faster' moving locations may impact the quality of coregistration and subsequently calculations of surface elevation change (dh/dt). To check that the dynamic thresholds we use do not strongly influence dh/dt solutions, we use Google Earth Engine to create an array of masked DEM mosaic datasets for nine different vertical and horizontal velocity configurations (Table S1). We use vertical velocity values from the Smith et al. (2020) mosaic that vary between 0.1 - 0.5 m/yr, and use a 1 - 10 m/yr threshold for horizontal velocity from MEaSUREs (Rignot et al., 2017). Each of the 9 masked REMA mosaic datasets is then used as a reference point cloud to coregister our set of DEM strips, following the methods described in section 2.1 of the main text. This produces 9 sets of DEM strips that we use to create 9 different maps of surface elevation change (dh/dt) utilizing the CARST package (Zheng et al., 2018). We compare the different mean rates of surface change that each solution provides, for each GNSS site (Table S1). The maximum spread in mean surface change rate is found at SLTR (1.72 m/yr). The majority of sites see differences less than 1 m/yr which provides us with confidence that we can utilize our least strict point cloud definition of 0.5 m/yr vertical velocity, and 10 m/yr horizontal, without affecting the results of our dh/dt.

For our finalized dh/dt grids we output dh/dt uncertainty maps (Figure S1). Volume change uncertainties are calculated following the methods of Zheng et al. (2018) and Melkonian et al. (2014) where we classify measurements from the same stack of DEMs as being mutually independent. Measurements from different DEM stacks are treated as independent. We group uncertainties by DEM stack and calculate bulk uncertainty using equation 4. from Zheng et al. (2018). Uncertainty maps can be found in Figure S1. For the uncertainties of Schroder et al. (2019) grid we use the uncertainty estimates provided by Schröder et al. (2019), and an estimated correlation length of 100 km (Nilsson et al., 2016).

Text S2. Geodetic Data Processing with GAMIT/GLOBK

We processed the ANET GPS data within a global network composed of ~2500 stations (with data spanning from 1993 to 2022, ~4 million station-days) using a parallelized Python wrapper for GAMIT/GLOBK v10.71 (Gómez, 2023). Processing of GPS data used the orbits and antenna calibration parameters available from the International GNSS Service (IGS14 reference frame), the Vienna Mapping Functions (Boehm et al., 2006) to estimate the atmospheric delays, and the ocean tide loading model FES2014b (Lyard et al., 2021).

Text S3. Station Trajectory Analysis and Reference Frame Realization

We use an automated procedure to fit trajectory models to the displacement time series of each CGPS station (Bevis & Brown, 2014; Bevis et al., 2019). This model is composed of up to 4 sub-models: a displacement trend (nearly always linear in time), a series of 0, 1 or more steps or Heaviside jumps, a seasonal displacement cycle, and,

when needed, logarithmic transients that accommodate transient displacements. Most trend models invoke constant velocity, but some invoke quadratic or higher order trends in order to account for accelerating patterns of displacement. The time of the jumps are imposed by us, but the amplitudes of these jumps are estimated. These jumps allow the model to incorporate coseismic displacements, and also coordinate discontinuities driven by changes in geodetic station equipment (mostly changes of antennas or radomes). Seasonal displacement cycles are modeled using a 4-term Fourier series (with annual and semi-annual periods). Our approach to modeling post-seismic transients followed the approach of Bevis et al. (2019) rather than that of Bevis and Brown (2014).

Reference frame (RF) realization and trajectory modeling are implemented simultaneously, so as to ensure internal geometrical consistency (Bevis & Brown, 2014). The horizontal aspect of the RF, in velocity or rate space, is imposed by minimizing the RMS horizontal velocities of a set of stations referred to as HREF. These stations are nominally part of the rigid portions of the Antarctica plate, in which there are no relative velocities driven by tectonics. The vertical aspect of the RF in velocity space is that which minimizes the RMS vertical velocities of a global set of CGPS stations called VREF. This set is chosen using the "ensemble of RFs" approach described by Bevis et al. (2013). The 16 HREF stations are VESL, SYOG, MAW1, DAV1, ABOA, BURI, LWN0, WHN0, ZHON, NONS, BRIP, BELG, COTE, FLM5 and BUMS in the Antarctic continent, and KERG in Kerguelen Island. The RMS horizontal velocity of these stations in the final ANET frame is 0.29 mm/yr. The RMS vertical velocity of the 850 VREF stations is 0.92 mm/yr. The station displacement time series and best-fit trajectory models referred to this RF are denoted as the geodetic solution pg03f_PC_H16.

Text S4. Mitigation of Icing Noise: Fine-Tuning the Trajectory Models for the Amundsen Sea Region Stations

All the trajectory models in the solution pg03f_PC_H16 were computed using default assumptions regarding the nature of the positioning noise. But many of the stations located along or near the Amundsen Sea Coast have time series containing highly structured and high amplitude artifacts driven by rime icing of the antenna and its radome and/or by invasion of the interior of the radome by fine ice crystals. Mitigating these large and highly systematic errors requires a customized analysis in which we remodel the time series making a range of decisions about the time window selected for modeling, which daily coordinate solutions are downweighted within this window because they are designated as outliers, and how the trajectory model is formulated. In adjusting the trajectory model we reconsider estimation of any displacement cycle, if a 4-term or a 2-term Fourier series should be used, and examine linear and quadratic trend models, keeping in mind that icing noise can produce much larger perturbations of a quadratic model relative to a time-linear trend model. We perform a range of experiments for each station, designate selected solutions as acceptable and identify a preferred solution, based on an a posteriori inspection of the results, the WRMS misfit, amongst other metrics. The formal standard errors for the preferred velocity estimates are adjusted upwards, if necessary, to accommodate the range of the velocity estimates in the other acceptable solutions.

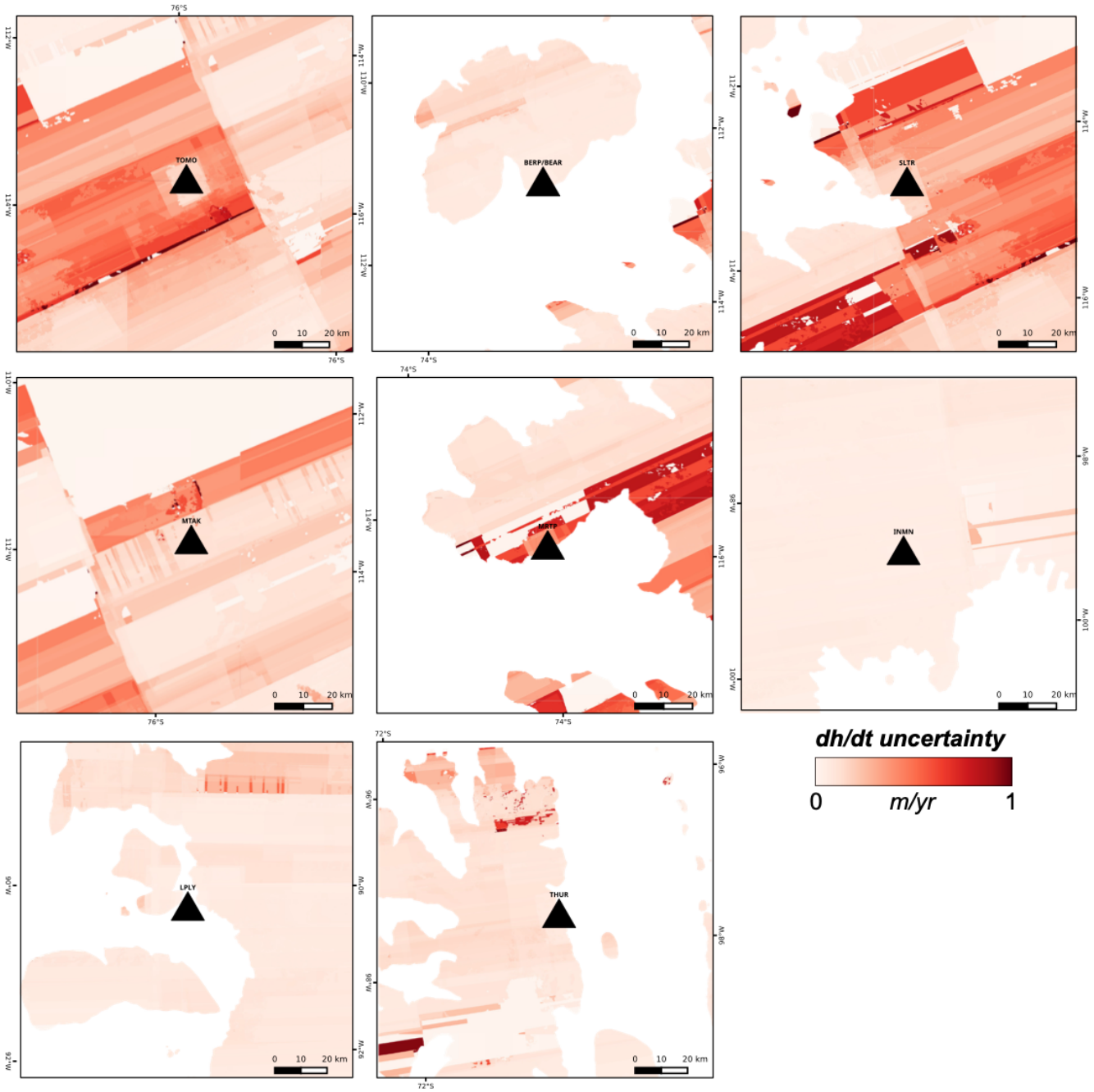

Figure S1. Grids of surface elevation change uncertainty produced at each GNSS site region following the methods of Zheng et al. (2018). Darker red regions have a greater associated uncertainty.

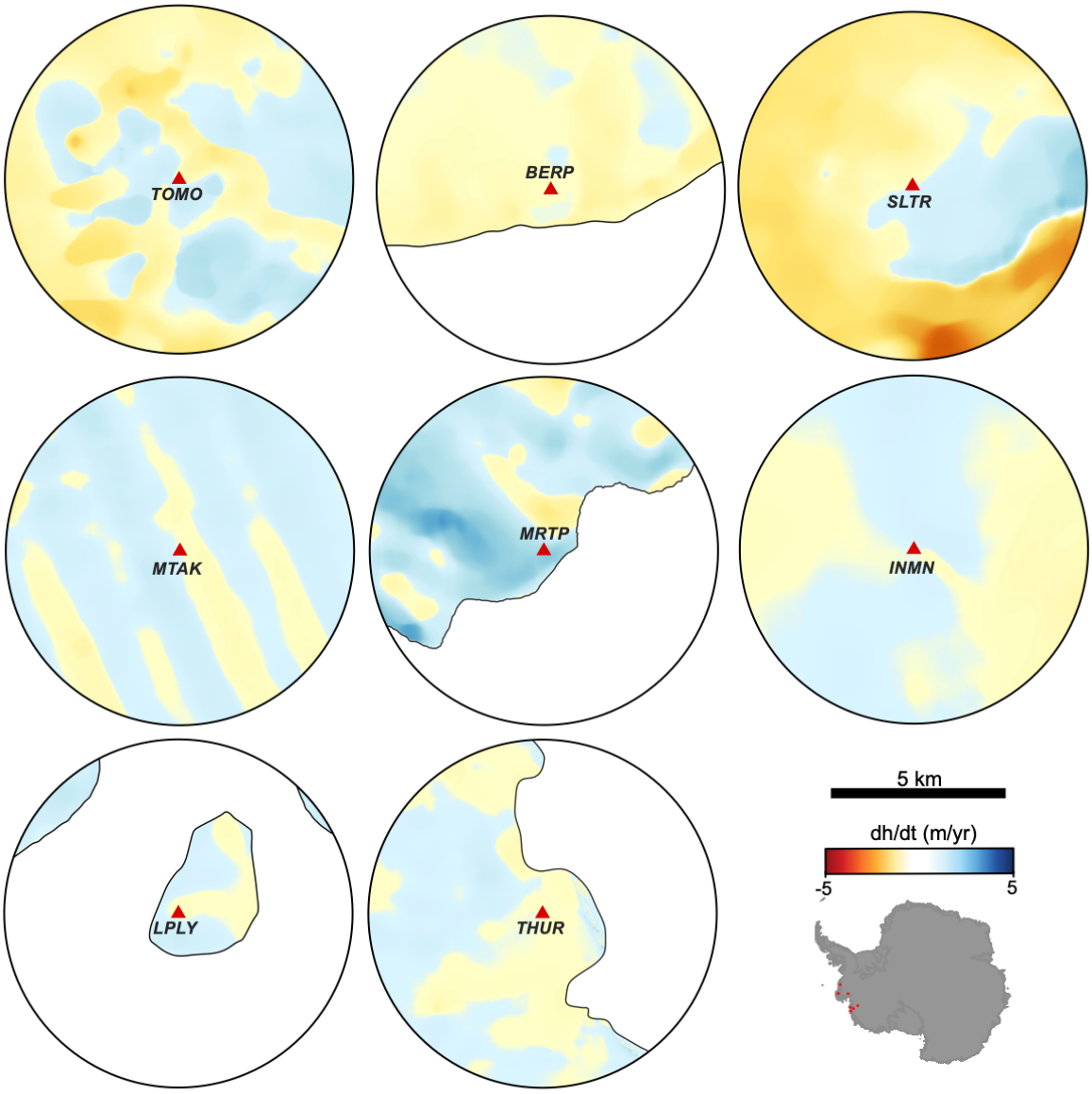

Figure S2. Surface elevation change (dh/dt) maps around each of the eight GNSS sites located in the Amundsen Sea Embayment Region. A 5 km radius around each site is marked on the figure to indicate the distance threshold outside of which there is a greatly reduced sensitivity to the resolution of your surface load change grid.

Table S1. Surface elevation change grids produced using DEM stacks coregistered to different dynamic point thresholds. For more information refer to Text S1.

Vertical velocity threshold (m/yr)		0.5	0.5	0.5	0.25	0.25	0.25	0.1	0.1	0.1	SPREAD (m/yr)
Horizontal velocity threshold (m/yr)		1	5	10	5	1	10	5	1	10	
mean dh/dt (m/yr)	BERP	-0.38	-0.38	-0.32	-0.12	-0.54	-0.11	-0.40	-0.45	-0.40	**0.54**
	INMN	-0.51	-0.49	-0.46	-0.26	-0.50	0.07	-0.51	-0.50	-0.50	**0.51**
	LPLY	-0.15	-0.15	-0.16	-0.71	-0.15	-0.51	-0.14	-0.16	-0.14	**0.71**
	MRTP	-0.15	0.00	0.09	-0.60	-0.36	0.41	-0.16	-0.44	-0.21	**0.60**
	MTAK	-0.15	0.00	0.09	-0.60	-0.36	0.41	-0.16	-0.44	-0.21	**0.60**
	SLTR	-1.63	-1.48	-1.65	0.00	-1.69	-0.20	-1.69	-1.72	-1.65	1.72
	THUR	0.08	0.05	0.04	0.46	0.08	0.38	0.05	0.07	0.04	0.04
	TOMO	-1.05	-0.97	-1.01	-0.39	-1.10	-0.45	-1.12	-1.19	-1.12	**1.19**

Table S2. GNSS solutions

Station	Vu	Su	Ve	Se	Vn	Sn
IGS_BERP	26.67	0.12	1.22	0.06	9.43	0.05
IGS_INMN	31.81	0.38	-2.55	0.2	7.22	0.21
IGS_LPLY	5.24	0.3	-1.07	0.19	-0.19	0.16
IGS_MRTP	14.12	0.57	0.4	0.2	4.17	0.16
IGS_MTAK	43.94	0.89	-2.38	0.21	-7.64	0.2
IGS_SLTR	49.65	1	-3.23	0.21	10.8	0.2
IGS_THUR	-2.86	0.11	-1.32	0.06	-2.63	0.06
IGS_TOMO	50.49	0.46	-5.86	0.16	-2.74	0.2

Caption for Table S3. Elastic modeling results for each directional component at each GNSS site for each surface load grid resolution and the three density scenarios.

Uncertainties are provided that capture the variability from 1000 model runs using a randomly sampled 1D elastic profile.

References

Bevis M., Brown, A., & Kendrick, E. (2013). Devising stable geometrical reference frames for use in geodetic studies of vertical crustal motion, *Journal of Geodesy,* 87, 311-321, https://doi.org/10.1007/s00190-012-0600-5.

Bevis, M., & Brown, A. (2014). Trajectory models and reference frames for crustal motion geodesy, *Journal of Geodesy,* 88, 283-311, https://doi.org/10.1007/s00190-013-0685-5.

Bevis, M., Bedford, J., & Caccamise II, D. (2019). The art and science of trajectory modeling. In J-P. Montillet, M. Bos (Eds.) *Geodetic Time Series Analysis in Earth Sciences* (pp. 1-28) https://doi.org/10.1007/978-3-030-21718-1_1.

Boehm, J., Niell, A., Tregoning, P., & Schuh, H. (2006). Global Mapping Function (GMF): A new empirical mapping function based on numerical weather model data. *Geophysical Research Letters, 33*(7), L07304. https://doi.org/10.1029/2005GL025546

Gómez, D. (2023*)* Parallel.GAMIT. [Software]. GitHub. https://github.com/demiangomez/Parallel.GAMIT

Howat, I. M., Porter, C., Smith, B. E., Noh, M.-J., & Morin, P. (2019). The Reference Elevation Model of Antarctica. *The Cryosphere, 13*(2), 665–674. https://doi.org/10.5194/tc-13-665-2019

Hughes, T. J. (1981). The weak underbelly of the West Antarctic ice sheet. *Journal of Glaciology, 27*(97), 518–525. https://doi.org/10.3189/s002214300001159x

Lyard, F. H., Allain, D. J., Cancet, M., Carrère, L., & Picot, N. (2021). FES2014 global ocean tides atlas: design and performances. *Ocean Science Discussions*, *17*(3),1–40. https://doi.org/10.5194/os-17-615-2021

Melkonian, A.K. (2014). *Quantifying and Characterizing Mass Loss From Icefields Using Remote Sensing* (Doctoral Dissertation). Retrieved from Cornell eCommons. (https://hdl.handle.net/1813/39298) Ithaca, NY: Cornell University.

Mouginot, J., Scheuchl, B., & Rignot, E. (2012). Mapping of Ice Motion in Antarctica Using Synthetic-Aperture Radar Data. *Remote Sensing, 4*(9), 2753–2767. https://doi.org/10.3390/rs4092753

Nilsson, J., Gardner, A., Sørensen, L. S., & Forsberg, R. (2016). Improved retrieval of land ice topography from CryoSat-2 data and its impact for volume-change

estimation of the Greenland Ice Sheet. *The Cryosphere, 10*(6), 2953–2969. https://doi.org/10.5194/tc-10-2953-2016

Rignot, E., Mouginot, J., & Scheuchl, B. (2011). Ice Flow of the Antarctic Ice Sheet. *Science, 333*(6048), 1427–1430. https://doi.org/10.1126/science.1208336

Rignot, E., Mouginot, J., & Scheuchl, B. (2017). MEaSUREs InSAR-Based Antarctica Ice Velocity Map (Version 2). [Dataset] NASA National Snow and Ice Data Center Distributed Active Archive Center. https://doi.org/10.5067/D7GK8F5J8M8R

Schröder, L., Horwath, M., Dietrich, R., Helm, V., Broeke, M. R. van den, & Ligtenberg, S. R. M. (2019). Four decades of Antarctic surface elevation changes from multi-mission satellite altimetry. *The Cryosphere, 13*(2), 427–449. https://doi.org/10.5194/tc-13-427-2019

Smith, B., Fricker, H. A., Gardner, A. S., Medley, B., Nilsson, J., Paolo, F. S., et al. (2020). Pervasive ice sheet mass loss reflects competing ocean and atmosphere processes. *Science*, *367*(6496), 1239-1242. https://doi.org/10.1126/science.aaz5845

Zheng, W., Pritchard, M. E., Willis, M. J., Tepes, P., Gourmelen, N., Benham, T. J., & Dowdeswell, J. A. (2018). Accelerating glacier mass loss on Franz Josef Land, Russian Arctic. *Remote Sensing of Environment,* 211, 357–375. https://doi.org/10.1016/j.rse.2018.04.004